Magnetic interactions in the catalyst used by nature to split water: a DFT + *U* multiscale study on the Mn_4CaO_5 core in photosystem II

Magnetic interactions in the catalyst used by nature to split water: a DFT + U multiscale study on the Mn$_4$CaO$_5$ core in photosystem II

Daniele Bovi[1]**, Daniele Narzi**[1] **and Leonardo Guidoni**[1,2,3]

[1] Dipartimento di Fisica, Sapienza–Università di Roma, piazzale Aldo Moro 5,
I-00185 Rome, Italy
[2] Dipartimento di Scienze Fisiche e Chimiche, Università degli Studi dell'Aquila, via Vetoio,
I-67100 L'Aquila, Italy
E-mail: leonardo.guidoni@univaq.it

Abstract

An important approach in the design of new environmentally friendly materials is represented by the study of analogous systems already existing in nature. In the search for new water splitting catalysts, the corresponding natural analogue is represented by the oxygen-evolving complex of photosystem II, which is a large membrane protein complex present in photosynthetic organisms. The understanding of the catalytic strategy of its active Mn$_4$CaO$_5$ core is important to unravel the mechanisms of water oxidation in photosynthesis and can serve as an inspiring model for the design of biomimetic catalysts based on largely non-toxic, earth abundant elements. The magnetic interactions between Mn ions are studied in the present work by means of DFT + U broken symmetry *ab initio* molecular dynamics within a quantum mechanics/molecular mechanics framework. The room temperature dynamics of two different structural models (i.e. with total high-spin and total low-spin ground states) was stable during the simulated time. We observed large fluctuations of the magnetic coupling

[3] Author to whom any correspondence should be addressed.

constants calculated on both the structural models of the complex, causing occasionally instantaneous swapping of the ferromagnetic/antiferromagnetic coupling between the metal centers.

[S] Online supplementary data available from stacks.iop.org/NJP/16/015020/mmedia

1. Introduction

Photocatalytic energy production by direct conversion of solar energy into a chemical fuel, such as hydrogen or hydrocarbons, is a major challenge in the research of new materials for energy. In particular, the discovery of new catalytic materials based on earth-abundant elements that are capable to perform the oxidation of water with high efficiency is a key ingredient for the future development of devices that are able to capture and store solar energy on a large scale [1]. Natural photosynthetic processes efficiently perform this task, capturing solar photons and converting them into chemical energy that can be stored in stable organic molecules. One of the most important steps in this process is represented by the oxidation of water, which is carried out by the oxygen evolving complex (OEC) of photosystem II (PSII), which is a protein/pigments complex that has remained almost evolutionary unchanged since its first appearance about 2.5 billion years ago [2]. The active site of the enzyme is composed of a core of four Mn ions and one Ca ion that are connected together through μ-oxo-bridges in an open cubane fashion [3]. In the last years, an inorganic cobalt-based catalyst film, having favorable working and stability conditions, was shown to be able to catalyze electrochemical water oxidation with small overpotential [4, 5]. The film is an amorphous solid that is self assembled from low cost cobalt salts at the anode. It has been recently combined with a silicon junction and with a hydrogen evolution catalyst to form a prototype 'artificial leaf' [6]. Interestingly, x-ray scattering measurements have revealed that the structure of this inorganic catalyst shares some common features with its natural counterpart [7–9].

Recently, Dau and co-workers [10, 11] have reported an Mn oxide that has also been characterized as water-oxidizing. The design of new materials based on Mn would be desirable since this element, which is that chosen by nature, is earth-abundant, inexpensive and largely non-toxic. Electronic structure calculations and *ab initio* molecular dynamics (MD) have been successfully used to unravel the structural and functional properties of molecular models of materials for water oxidation based on transition metals [12–14]. These studies are important to understand the similarities and differences of the electronic properties of the catalysts and they might also help in the design of new biomimetic materials, when compared to parallel studies on natural enzymes.

A high-resolution crystallographic structure of the PSII complex has recently revealed the atomistic details of the catalytic Mn_4CaO_5 core [3]. This structure provides the grounds for parallel computational investigations of the catalytic mechanism of the OEC [15–18]. It also helps the study of natural and synthetic analogous for water splitting reactions [9]. During the catalytic pathways toward oxygen evolution, the natural system cycles through different states, which are the S_0–S_4 states of the so-called Kok's Cycle [19]. Despite a large amount of data being available for the functional and spectroscopic properties of such states in different organisms and experimental conditions [20–23], the exact reaction mechanism and the strategy adopted by the enzyme to carry on its task are still elusive. An important aspect of the OEC,

as well as of their artificial analogues, is represented by the magnetic interactions between the transition metals connected by oxo-bridges. In this respect, electronic paramagnetic resonance is successfully and routinely used to probe the oxidation state and the chemical environment of the PSII core along the Kok's cycle and its intermediates [21]. From the computational point of view, the description of such magnetic states can be conveniently described through broken-symmetry (BS) approach based on density functional theory (DFT) [24–29]. In a recent work, Pantazis *et al* [18] have proposed two distinct gas-phase (GP) molecular models of the Mn_4CaO_5 cluster in PSII, differing by the magnetic interactions between Mn ions. These two structures have two different overall spin ground states and their interconversion can explain the presence of two distinct signals observed by EPR spectroscopy in the S_2 state [20, 21, 30, 31]. Two important factors should be considered to fully describe the interplay of such magnetic interactions in biologically relevant conditions, which are: the effect of temperature and the role of the protein field. To achieve this goal, *ab initio* MD simulations coupled to quantum mechanics/molecular mechanics (QM/MM) scheme can be used to unravel both the effect of dynamics and the effect of the environment on the average values and fluctuations of the magnetic properties [32]. To properly describe the electron correlation of the transition metal centers, it is necessary to go beyond the approximations used by the standard DFT, either with the use of hybrid functionals or with the DFT+U scheme [33–37]. Since the latter approach is particularly computationally efficient for *ab initio* MD calculations, it has been adopted for the present study.

In this work, we present a QM/MM study of the Mn_4CaO_5 cluster of PSII carried on at the DFT+U level for both the low-spin and the high-spin proposed structures. Our extensive analysis will reveal the role of the temperature and of the protein field in the modulation of the magnetic interactions in the PSII catalytic core.

2. Materials and methods

The portion of the system close to the active site was treated by DFT as an isolated cluster (GP calculations) or immersed into its protein environment (QM/MM calculations). As suggested by Pantazis *et al* [18], for both calculations we have considered two different configurations of the cluster, which are hereafter referred to as model-A and model-B, differing by the oxidation and spin pattern of the Mn ions as detailed below.

2.1. Gas-phase model

The GP model was defined consistently with the DFT calculations that were previously reported for the S_2 state [18, 31, 38]. The system is shown in left panel of figure 1, and it is composed by 238 atoms: the metal core (Mn_4CaO_5), the side chains of its ligands (Asp170, Glu189, His332, Glu333, Asp342, Ala344, and CP43-Glu354), their neighbors residues (Asp61, Tyr161, His190, CP43-Arg357 and His337), the two water molecules coordinated to the Ca^{2+}, a H_2O plus an OH^- bound to the terminal Mn4 (see also figure 2), and the closest eight crystallographic water molecules (not shown for clarity in figure 1).

In agreement with a previous study [18] we defined and investigated two different conformers of the catalytic core in S_2 state (see figure 2), the GP model-A (GP-A) and the GP model-B (GP-B). The geometries of these two models differ from each other by the position of an oxo-bridge (O5) which is bound in one case to Mn4 (model-A) and in the other case to
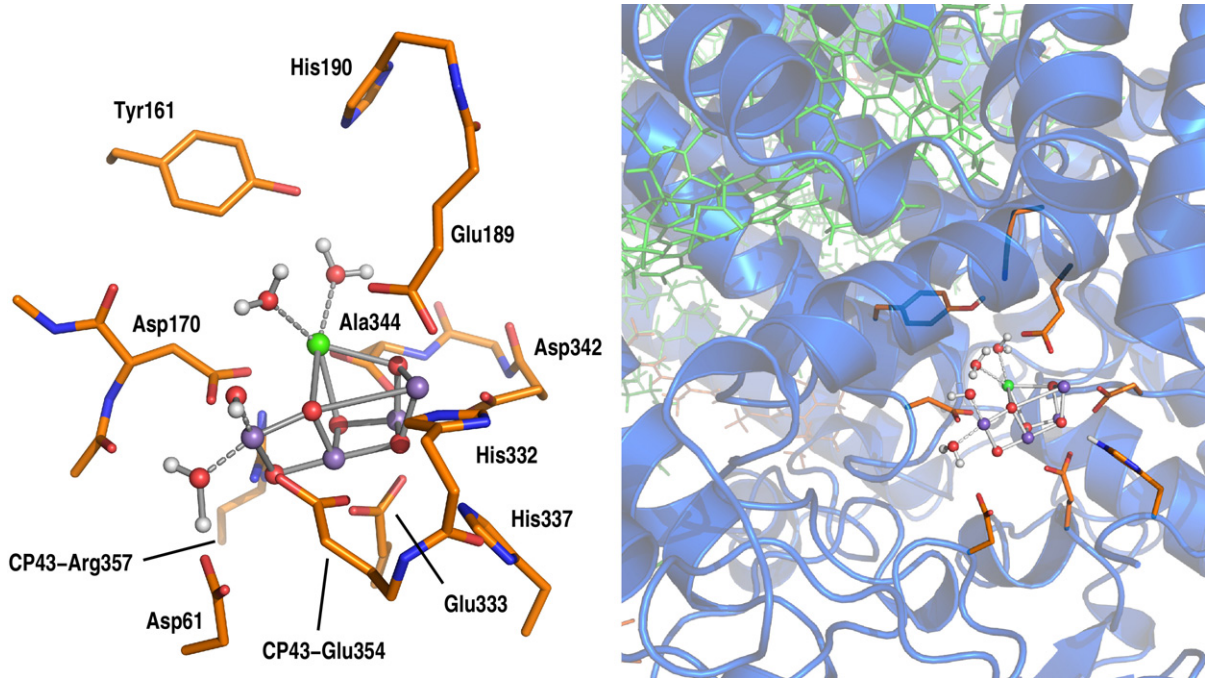
Figure 1. Selected atoms from the molecular models of the catalytic center of the OEC used for the DFT calculations in GP (left panel) and QM/MM calculations (right panel). A detailed description of the atoms considered in both models is reported in section 2. The Mn$_4$CaO$_5$ cluster is shown by a ball-and-stick representation (Mn purple, Ca green, O red and H white), while the other residues included in the QM part are reported with sticks. In the right panel, the portion of the system treated at classical level is shown in cartoon representation (protein residues) and in green sticks (chlorophylls).

Mn1 (model-B). Consequently, the oxidation states of the Mn1 and Mn4 in the two models differ according to the respective coordination pattern (i.e. Mn1(III) Mn4(IV) in model-A and Mn1(IV) Mn4(III) in model-B).

From the electronic structure point of view, the electron open-shell Mn$_4$CaO$_5$ cluster is composed by one Mn^{III} and three Mn^{IV}, with four and three unpaired electrons, respectively. These electrons occupy the quasi-degenerate d-like orbitals, localized close to the metallic center, and they give rise to a local high-spin configuration on each metal center. However, due to the exchange and super-exchange interactions, the alignment (parallel or antiparallel) between the resulting spins of each Mn ion is strongly sensitive to the structural parameters of the Mn$_4$CaO$_5$, thus changing from model-A to model-B. The exchange interactions between the electrons of the Mn ions and the energy spin ladder can be described at a phenomenological level by the Heisenberg Hamiltonian

$$\hat{H} = -2 \sum_{i,j(i>j)} J_{ij} \hat{S}_i \hat{S}_j, \tag{1}$$

where $\hat{S}_i$ and $\hat{S}_j$ are the spin operators of the resulting magnetic momentum on the metal center i and j, whereas J_{ij} represents their exchange coupling constant. In order to describe the electronic states using a single Slater-determinant in DFT, we use the BS approach that leads to a good description of the electron density and allows an estimation of the exchange coupling
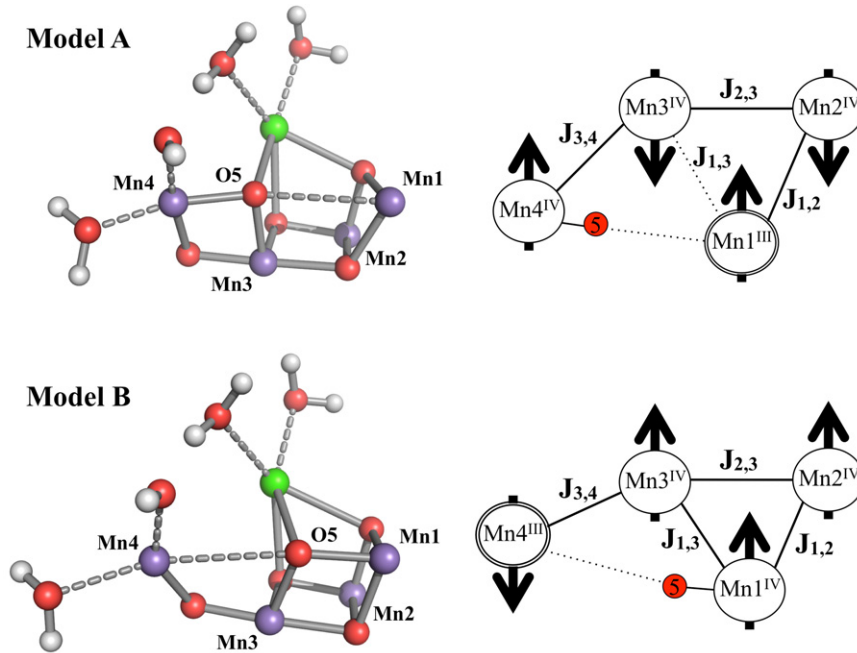
Figure 2. Structural and magnetic features of model-A and model-B. On the left, the Mn_4CaO_5 cluster for the two models is shown in a ball-and-stick representation. The right panel describes the configuration of the ground spin state for the two models. The up and down arrows indicate the spin projection, whereas the Roman numerals refer to the formal oxidation state of the four Mn atoms.

constants J_{ij} [39–41]. In the four-metal core Mn_4CaO_5, one total high-spin state and seven BS states with different multiplicities have to be calculated in order to evaluate the exchange coupling constants between the four manganese atoms (see the supplementary data, available from stacks.iop.org/NJP/16/015020/mmedia).

The DFT calculations were performed using the ORCA [42] and CP2K [43] packages. In the ORCA calculations, the all-electron Ahlrichs TZVP basis set [44] and def2-TZVP/J auxiliary basis sets [45] are employed for all atoms, except for the C and H atoms that are described with SVP and SVP/J. We used the B3LYP hybrid functional [46–48], which has already been used to reproduce accurate energetics and magnetic properties for manganese complexes [29]. To investigate the effect of a polarizable environment, we also used an implicit solvent model (with dielectric constant $\epsilon = 8$), as implemented in [49]. In the calculations performed with CP2K, all of the atoms are described by the GTH pseudo-potentials [50, 51]. The DZVP-MOLOPT-SR-GTH basis set, optimized for molecular systems, is employed for all atoms. For the B3LYP calculations, the SZV-MOLOPT-SR-GTH auxiliary basis set is used for the Mn and Ca atoms and the cFIT3 is used for the other atoms [43].

In order to reduce the computational cost in *ab initio* MD simulations, we have adopted the DFT+U scheme [33, 52, 53]. This approach uses a basic density functional (i.e. the generalized gradient corrected PBE functional [54] in our case), including in the KS orbitals calculation an Hubbard correction term (inspired to the Hubbard model) that acts on the *d* orbitals of the Mn atoms. This Hubbard correction is system dependent and it is defined by the effective parameter U as detailed in the supplementary data. The value of the parameter U was chosen in order

to reproduce the J_{ij} values obtained by the B3LYP functional on two reference geometries. The final value $U = 1.16\,\text{eV}$ was derived from the average of the linear interpolations on the exchange coupling constants J_{ij}, as explained in detail in the supplementary data.

2.2. Quantum mechanics/molecular mechanics model

The starting structure of the oxygen-evolving PSII at 1.9 Å resolution was taken from the protein data bank (PDB ID: 3ARC, [3]). The AMBER99SB force field [55] was used to describe the protein residues whereas the topologies describing the other molecules present in the crystal structure are based on the general AMBER force field [56] and generated using the Antechamber software [57] (for further detail see the supplementary data). The x-ray structure was embedded into a membrane bilayer that was composed of DOPC lipids [58] and solvated in TIP3p water molecules [59]. The total classical system consists of almost 650 000 atoms. Three nanoseconds of MD simulation with harmonic position restraints on the heavy atoms of the protein, cofactors and crystal waters at constant volume and temperature ($T = 298\,\text{K}$) were performed, followed by 3 ns of MD simulation with the same harmonic position restraints in NPT ensemble ($T = 298\,\text{K}$ and $P = 1\,\text{bar}$). MD simulations were carried out using the GROMACS software package [60, 61]. Further details are reported in the supplementary data (see the supplementary data, available from stacks.iop.org/NJP/16/015020/mmedia).

Starting from the last step of the position restrained trajectory in NPT ensemble, we cropped a portion of the system consisting of the Mn_4CaO_5 cluster plus the closest protein domains (i.e. D1, D2 and CP43), and the nearby cofactors and water molecules. The coordinates of the Mn_4CaO_5 cluster and the four directly coordinated water molecules were modified using the geometries suggested by Patanzis *et al* [18] for the S_2 state of the Kok's cycle (model-A and model-B). Both models were optimized using the CP2K package in a mixed quantum/classical approach [62]. The metal core, its ligands (Asp170, Glu189, His332, Glu333, Asp342, Ala344 and CP43-Glu354), their closest residues (Asp61, Tyr161, His190, His337, Ser169 and CP43-Arg357), the ten closest water molecules plus the four water molecules coordinated to the Mn_4CaO_5 cluster and the chloride anion next to Glu333 were treated at DFT level, as described in the previous sections, whereas the remaining part of the system was described by a classical force field. The electrostatic coupling between the quantum and the classical portion of the system were treated using fast Gaussian expansion of the electrostatic potential as implemented in the CP2K package [43].

The QM/MM MD were performed in NVT ensemble at a temperature of 298 K using the Nosé–Hoover thermostat [63–65] to couple the system with a double thermal bath (one for the MM system and the other for the QM system), both with a time constant of 0.1 ps. The cutoff for the plane-wave expansion was set to 280 Ryd in the QM cell, with dimensions 26.5, 26.0 and 28.0 Å. QM/MM MD simulations were performed in a PBE+U scheme [33, 52, 53] for the QM part, as described before. The same basis set that was adopted in the GP calculations was employed. Positions of the classical C_α atoms were kept fixed during the dynamic. Both QM/MM MD simulations were set up in their suggested ground spin states (total spin $S = 1/2$ for the model-A and $S = 5/2$ for the model-B) with relative spin orientations of the Mn atoms in agreement with previous works [18, 31]. The two simulations ran for 10.0 ps, 7.5 of which have been used for data production.

Table 1. Comparison of the main distances (Å) and angles (degree) in Mn_4CaO_5 cluster between the XRD structure [3] and model-A and model-B in GP and in the QM/MM description, optimized in their respective spin ground-state and averaged over 10 ps of simulation MD. The standard deviations are reported in brackets.

	Model-A			Model-B			
	GP-OPT	QM/MM OPT	QM/MM MD	GP-OPT	QM/MM OPT	QM/MM MD	XRD[a]
Mn1–Mn2	2.78	2.82	2.79 (0.07)	2.74	2.75	2.78 (0.06)	2.8
Mn1–Mn3	3.35	3.34	3.37 (0.11)	2.93	2.97	2.94 (0.07)	3.3
Mn2–Mn3	2.80	2.77	2.81 (0.07)	2.80	2.76	2.82 (0.06)	2.9
Mn3–Mn4	2.82	2.78	2.77 (0.06)	3.21	3.06	3.15 (0.12)	2.9
Mn1–Ca	3.62	3.58	3.61 (0.12)	3.44	3.40	3.40 (0.11)	3.5
Mn2–Ca	3.39	3.37	3.39 (0.12)	3.47	3.42	3.43 (0.12)	3.3
Mn3–Ca	3.50	3.36	3.58 (0.15)	3.47	3.30	3.45 (0.14)	3.4
Mn4–Ca	3.98	3.59	3.83 (0.13)	4.22	3.78	3.99 (0.16)	3.8
Mn1–O5	3.16	3.05	3.07 (0.21)	1.84	1.89	1.88 (0.07)	2.6
Mn4–O5	1.93	1.89	1.87 (0.06)	3.27	3.12	3.14 (0.18)	2.5
Mn1–MMn4	5.05	4.92	4.89 (0.19)	5.09	5.00	5.00 (0.18)	5.0
Mn3–oxo–Mn4	99/97	96.3/97.5	96.3/96.5 (3.1/3.1)	125	114.9	117.6 (6.6)	96/95
Mn1–oxo–Mn4	97/92	98.2/92.9	98.0/92.2 (3.2/3.1)	95/91	96.7/91.5	97.7/92.7 (3.0/2.9)	97/93
Mn1–oxo–Mn3	116	116.2	117.2 (5.6)	102/97	104.0/99.1	102.2/97.6 (3.6/3.6)	118
Mn2–oxo–Mn3	99/90	97.4/90.4	99.2/90.6 (3.1/3.1)	100/90	97.2/90.3	99.3/91.0 (3.2/3.0)	99/91

[a] Average values of the two monomers.

3. Results and discussion

On the basis of the models proposed by Pantazis *et al* [18], we built GP models of the two conformers that were representative of the S_2 state of the Kok's cycle proposed to be interconvertible in the PSII structure. The two geometries differ mainly by the position of the oxygen O5, which is bound to Mn4 in model-A, whereas in model-B it is bound to Mn1, as shown in figure 2. The two models have different magnetic properties, which are: an overall low-spin configuration for model-A, which is represented by a BS state of multiplicity 2, and an overall high-spin configuration for model-B, which is described by a BS state with multiplicity 6 (see the right panel of figure 2).

Upon geometry optimization, we calculated all the J_{ij} coupling constants using different functionals (table S2 of the supplementary data (see the supplementary data, available from stacks.iop.org/NJP/16/015020/mmedia)). The B3LYP Hybrid functional, which has been shown to fairly reproduce coupling constants in Mn dimers [29], provides a trend that is similar to that obtained following the procedure of [18]. This has been taken as reference for the choice of the parameter U for the Hubbard correction in PBE + U calculations. The optimal choice of the U value has been taken by fitting the J_{ij} parameters on the B3LYP reference for both model-A and model-B, following the procedure detailed in the supplementary data (see also table S3). The resulting value $U = 1.16$ eV is, therefore, used in all of the following DFT + U calculations.

For both the high-spin(A) and the low-spin(B) states, we report in table 1 the geometrical parameters of the optimized GP models, the optimized QM/MM models, and the averaged values along the QM/MM dynamics. Although it has been pointed out that the cluster geometry is affected by x-ray radiation damage [3, 38], in the last column distances and angles measured

Table 2. A comparison of the exchange coupling constants calculated on the optimized GP structure (GP-OPT), on the optimized QM/MM structure (QM/MM-OPT) and averaged over 50 snapshots extracted from the QM/MM MD trajectory (QM/MM-MD). Optimizations of model-A and model-B were carried out in the respective spin ground states. $J_{1,4}$ and $J_{2,4}$ (marked in gray) should be considered physically unmeaningful because they refer to Mn ions not linked by a μ-oxo-bridge.

	Model-A			Model-B		
	GP-OPT	QM/MM-OPT	QM/MM-MD	GP-OPT	QM/MM-OPT	QM/MM-MD
$J_{1,2}$	−13.6	−6.7	−11.2 (1.1)	25.3	28.1	27.9 (1.6)
$J_{1,3}$	4.3	4.0	1.9 (0.5)	14.3	14.6	21.3 (1.6)
$J_{1,4}$	1.1	3.9	4.5 (0.6)	3.2	5.8	5.2 (0.6)
$J_{2,3}$	27.8	15.4	20.8 (1.6)	33.7	24.1	22.3 (1.7)
$J_{2,4}$	1.8	3.0	2.9 (0.1)	1.5	1.1	1.1 (0.1)
$J_{3,4}$	−12.2	−7.3	−12.4 (1.9)	−31.9	−7.8	−8.2 (2.7)

in the x-ray diffraction (XRD) structure [3] are shown for comparison. As expected, the main difference between the distances found in the x-ray structure and those of the A and B models arises from the Mn1–O5 and the Mn4–O5 distances. The O5 atom, which is equidistant from the two manganese ions in the crystallographic structure, in our models is clearly bound to only one manganese ion (Mn4 for model-A and to Mn1 for model-B).

With respect to the GP optimized geometries, the QM/MM relaxed structures display two main differences: a reduced distance between Mn4 and the Ca ion (about 0.4 Å in both models, and a slightly shorter distance between Mn1 and Mn4, which is reflected in a shorter distance between O5 and the Mn that is not bound to it. Whereas the first effect is attenuated by the dynamics, the second remains basically unchanged at finite temperature. As a general remark, we observe that the overall structures remain fairly stable along the simulated time. In particular, the bond distances between the Mn atoms of the cluster remain close to the optimized structure values with fluctuations about 0.1 Å, with the exception of the Mn1–Mn4 distance that experienced rather larger fluctuations due to a reduced rigidity of the Mn4 connection with respect to the cubane structure. Both the enhanced mobility of O5 and its delocalization in QM/MM simulations might suggest a possible role of the protein field to promote the transition from model-A to model-B. This issue can have important implications since the O5 oxo-bridge atom is thought to be a substrate for the molecular oxygen formation catalyzed by the PSII [66, 67]. An improved protein-assisted mobility might, therefore, be relevant to understand the molecular mechanism behind water oxidation.

The magnetic coupling constants have been calculated on the QM/MM optimized structures as well as along the MD trajectories. As shown previously [18], the calculated J coupling constants for the two investigated models are consistent with a large amount of EPR experiments. The comparison between the GP and QM/MM single point calculations are reported in table 2. Interestingly, in model-A the physically meaningful J_{ij} values (i.e. $J_{1,2}$ $J_{1,3}$ $J_{2,3}$ $J_{3,4}$, since the respective atom pairs are connected by oxo bridges) calculated on the QM/MM optimized structure show weaker ferromagnetic and antiferromagnetic interactions with respect to the GP model. Thermal fluctuations act on the magnetic coupling constants, increasing both the ferromagnetic and the antiferromagnetic interactions when compared to the values calculated on the optimized QM/MM structure. In the case of model-B, the differences
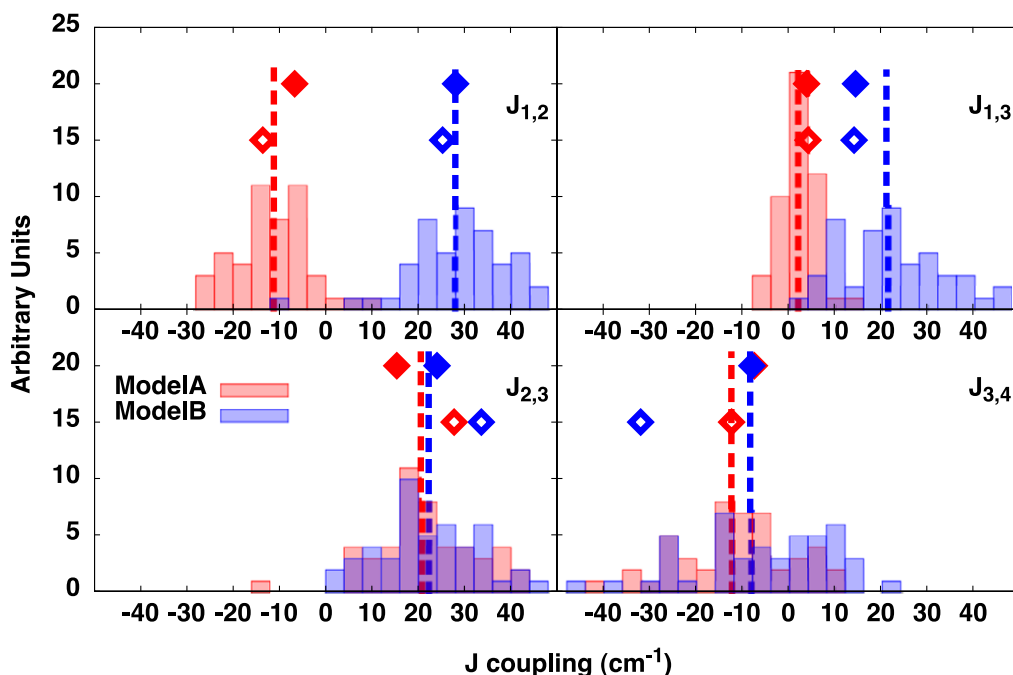
Figure 3. Histograms of the exchange coupling constants J_{ij} as obtained along the QM/MM MD trajectories at room temperature of model-A (red) and model-B (blue). The average value of each distribution is represented by the dotted lines. The J_{ij} values calculated on the optimized (zero temperature) structures are shown as single color-filled diamonds for the QM/MM system and as empty diamonds for the GP model.

between the J_{ij} values evaluated on the single QM/MM optimized structure and averaged over the QM/MM trajectory are smaller when compared to the trend found in model-A. In particular, only the $J_{1,3}$ value differs substantially when the effect of the dynamics at finite temperature is explicitly taken in account. Moreover, in the case of model-B, the QM/MM calculation, independently on the inclusion of the dynamics, decreases the magnetic interactions between Mn2 and Mn3 and between Mn3 and Mn4 with respect to the GP calculations. In particular, as shown in figure 3 and table 2, we found that $J_{3,4}$ in model-B largely depends on whether the GP models or QM/MM simulations are considered. The reasons for this effect can be attributed to the high mobility of Mn4, which is external to the cubane structure. The small variations of its distance and angle parameters can easily largely affect the value of the $J_{3,4}$ coupling constant.

Apart from the average J_{ij} values, another important information available from a dynamical description of the system concerns the fluctuations of the coupling constants due to the thermal motions. An histogram of the coupling parameters calculated along the QM/MM trajectories is shown in figure 3. It is interesting to point out that the fluctuations of the coupling constants are remarkably large, often being about half of the average signal. The points on the tail of the J_{ij} are often rather off their average values, even instantaneously inverting the sign of the magnetic coupling: from antiferromagnetic to ferromagnetic (as in the case of $J_{3,4}$ in both model-B and model-A) and from ferromagnetic to antiferromagnetic (e.g. $J_{2,3}$ in model-A, $J_{1,2}$ in model-B).

These fluctuations, changing instantaneously the kind of the magnetic interaction between manganese atoms, might have important consequences on the interconversion between the two

structures and on the catalytic mechanism of the Mn_4CaO_5 cluster. In particular, it is thought that a specific spin configuration for the manganese atoms, as well as for the oxygen atoms involved in the formation of the O_2 molecule, is required in order to allow the water splitting reaction [66]. A proper (dynamical) description of the spin electron density of the Mn_4CaO_5 cluster in the QM/MM scheme, which takes into account both the biological environment and the thermal fluctuations, is crucial in order to fully characterize the two structures model-A and model-B and to understand their role in the S_2–S_3 transition. On the basis of similar calculations, in a recent work [31] we have provided a framework in which it is possible to interpret several puzzling EPR experiments that identified metastable states between S_2 and S_3.

4. Conclusions

In the present work we have investigated the structural and magnetic properties of the Mn_4CaO_5 catalytic core of PSII. Thanks to the use of DFT+U framework within BS approach, we were able to describe the electronic structure and the magnetic properties of both model-A (low spin) and model-B (high spin) of the PSII in S_2 state. The two systems, simulated at room temperature, were structurally stable during the simulated dynamics. The magnetic coupling constants calculated on snapshots along dynamics show large fluctuations in both models, especially for $J_{3,4}$, which is the most sensitive to structural changes. The thermal fluctuations are so large that they induce instantaneous swapping between antiferromagnetic and ferromagnetic interactions, even in the case of largest $|J_{ij}|$ values. These effects might suggest that the relative stabilities of high-spin and low-spin surfaces in both model-A and model-B can be instantaneously inverted; therefore, facilitating surface hopping between the two spin states. Despite this broad distribution, their average values were in general close to that calculated on QM/MM optimized structures. In addition, the present work demonstrates the possibility of performing QM/MM MD simulations with an accurate treatment of the Mn–Mn interactions. The use of such methodologies opens the way to the study of the water splitting mechanisms in PSII within a framework that takes into account the effects of temperature fluctuations and of the protein environment.

Acknowledgments

References

[1] Faunce T *et al* 2013 Artificial photosynthesis as a frontier technology for energy sustainability *Energy Env. Sci.* **6** 1074–6
[2] Barber J 2008 Photosynthetic energy conversion: natural and artificial *Chem. Soc. Rev.* **38** 185
[3] Umena Y, Kawakami K, Shen J-R and Kamiya N 2011 Crystal structure of oxygen-evolving photosystem II at a resolution of 1.9 Å *Nature* **473** 55–65
[4] Kanan M W and Nocera D G 2008 *In situ* formation of an oxygen-evolving catalyst in neutral water containing phosphate and Co^{2+} *Science* **321** 1072–5

[5] Kanan M W, Surendranath Y and Nocera D G 2009 Cobalt phosphate oxygen-evolving compound *Chem. Soc. Rev.* **38** 109–14

[6] Nocera D G 2012 The artificial leaf *Account. Chem. Res.* **45** 767–76

[7] Dau H, Grundmeier A, Loja P and Haumann M 2008 On the structure of the manganese complex of photosystem II: extended-range EXAFS data and specific atomic-resolution models for four S-states *Phil. Trans. R. Soc.* B **363** 1237–43

[8] Risch M, Khare V, Zaharieva I, Gerencser L, Chernev P and Dau H 2009 Cobalt-oxo core of a water-oxidizing catalyst film *J. Am. Chem. Soc.* **131** 6936–7

[9] McAlpin J G, Stich T A, Casey W H and Britt R D 2012 Comparison of cobalt and manganese in the chemistry of water oxidation *Coord. Chem. Rev.* **256** 2445–52

[10] Zaharieva I, Najafpour M M, Wiechen M, Haumann M, Kurz P and Dau H 2011 Synthetic manganese-calcium oxides mimic the water-oxidizing complex of photosynthesis functionally and structurally *Energy Env. Sci.* **4** 2400–8

[11] Zaharieva I, Chernev P, Risch M, Klingan K, Kohlhoff M, Fischer A and Dau H 2012 Electrosynthesis, functional and structural characterization of a water-oxidizing manganese oxide *Ener. Env. Sci.* **5** 7081–9

[12] Mattioli G, Risch M, Bonapasta A A, Dau H and Guidoni L 2011 Protonation states in a cobalt-oxide catalyst for water oxidation: fine comparison of *ab initio* molecular dynamics and x-ray absorption spectroscopy results *Phys. Chem. Chem. Phys.* **13** 15437–41

[13] Ma C, Piccinin S and Fabris S 2012 Reaction mechanisms of water splitting and H_2 evolution by a Ru(II)–Pincer complex identified with *ab initio* metadynamics simulations *ACS Catal.* **2** 1500–6

[14] Hu X L, Piccinin S, Laio A and Fabris S 2012 Atomistic structure of cobalt-phosphate nanoparticles for catalytic water oxidation *ACS Nano* **6** 10497–504

[15] Luber S, Rivalta I, Umena Y, Kawakami K, Shen J-R, Kamiya N, Brudvig G W and Batista V S 2011 S_1-state model of the O_2-evolving complex of photosystem II *Biochemistry* **50** 6308–11

[16] Rivalta I *et al* 2011 Structural–functional role of chloride in photosystem II *Biochemistry* **50** 6312–5

[17] Siegbahn P E M 2012 Mechanisms for proton release during water oxidation in the S2–S3 and S3–S4 transitions in photosystem II *Phys. Chem. Chem. Phys.* **14** 4849–56

[18] Pantazis D A, Ames W, Cox N, Lubitz W and Neese F 2012 Two interconvertible structures that explain the spectroscopic properties of the oxygen-evolving complex of photosystem II in the S2 state *Angew. Chem. Int. Edn Engl.* **51** 9935–40

[19] Kok B, Forbush B and McGloin M 1970 Cooperation of charges in photosynthetic O_2 evolution *Photochem. Photobiol.* **11** 457–75

[20] Boussac A, Un S, Horner O and Rutherford A W 1998 High-spin states ($S \geqslant 5/2$) of the photosystem II manganese complex *Biochemistry* **37** 4001–7

[21] Haddy A 2007 EPR spectroscopy of the manganese cluster of photosystem II *Photosynth. Res.* **92** 357–68

[22] Styring S, Sjoholm J and Mamedov F 2012 Two tyrosines that changed the world: interfacing the oxidizing power of photochemistry to water splitting in photosystem II *BBA-Bioenergetics* **1817** 76–87

[23] Dau H, Zaharieva I and Haumann M 2012 Recent developments in research on water oxidation by photosystem II *Curr. Opin. Chem. Biol.* **16** 3–10

[24] Schreiner E, Nair N N, Pollet R, Staemmler V and Marx D 2007 Dynamical magnetostructural properties of Anabaena ferredoxin *Proc. Natl Acad. Sci. USA* **104** 20725–30

[25] Nair N N, Schreiner E, Pollet R, Staemmler V and Marx D 2008 Magnetostructural dynamics with the extended broken symmetry formalism: antiferromagnetic [2Fe–2S] complexes *J. Chem. Theory Comput.* **4** 1174–88

[26] Neese F 2004 Definition of corresponding orbitals and the diradical character in broken symmetry DFT calculations on spin coupled systems *J. Phys. Chem. Solids* **65** 781–5

[27] Neese F 2009 Prediction of molecular properties and molecular spectroscopy with density functional theory: from fundamental theory to exchange-coupling *Coord. Chem. Rev.* **253** 526–63

[28] Orio M, Pantazis D A, Petrenko T and Neese F 2009 Magnetic and spectroscopic properties of mixed valence manganese (III, IV) dimers: a systematic study using broken symmetry density functional theory *Inorg. Chem.* **48** 7251–60

[29] Bovi D and Guidoni L 2012 Magnetic coupling constants and vibrational frequencies by extended broken symmetry approach with hybrid functionals *J. Chem. Phys.* **137** 114107

[30] Boussac A, Girerd J-J and Rutherford A W 1996 Conversion of the spin state of the manganese complex in photosystem II induced by near-infrared light *Biochemistry* **35** 6984–9

[31] Bovi D, Narzi D and Guidoni L 2013 The S2 state of the oxygen-evolving complex of photosystem II explored by QM/MM dynamics: spin surfaces and metastable states suggest a reaction path towards the S3 state *Angew. Chem. Int. Edn Engl.* **52** 11744–9

[32] Colombo M C, VandeVondele J, Van Doorslaer S, Laio A, Guidoni L and Röthlisberger U 2008 Copper binding sites in the C-terminal domain of mouse prion protein: a hybrid (QM/MM) molecular dynamics study *Proteins* **70** 1084–98

[33] Anisimov V I, Zaanen J and Andersen O K 1991 Band theory and Mott insulators: Hubbard U instead of Stoner I *Phys. Rev.* B **44** 943–54

[34] Anisimov V I, Aryasetiawan F and Lichtenstein A I 1997 First-principles calculations of the electronic structure and spectra of strongly correlated systems: the LDA+U method *J. Phys.: Condens. Matter* **9** 767–808

[35] Pickett W E, Erwin S C and Ethridge E C 1998 Reformulation of the LDA + U method for a local orbital basis *Phys. Rev.* B **58** 1201–9

[36] Kulik H J, Cococcioni M, Scherlis D A and Marzari N 2006 Density functional theory in transition-metal chemistry: a self-consistent Hubbard U approach *Phys. Rev. Lett.* **97** 103001

[37] Franchini C, Podloucky R, Paier J, Marsman M and Kresse G 2007 Ground-state properties of multivalent manganese oxides: density functional and hybrid density functional calculations *Phys. Rev.* B **75** 195128

[38] Ames W, Pantazis D A, Krewald V, Cox N, Messinger J, Lubitz W and Neese F 2011 Theoretical evaluation of structural models of the S-2 state in the oxygen evolving complex of photosystem II: protonation states and magnetic interactions *J. Am. Chem. Soc.* **133** 19743–57

[39] Noodleman L 1981 Valence bond description of antiferromagnetic coupling in transition metal dimers *J. Chem. Phys.* **74** 5737–43

[40] Yamaguchi K, Fukui H and Fueno T 1986 Molecular-orbital (MO) theory for magnetically interacting organic-compounds *Chem. Lett.* **4** 625–8

[41] Shoji M, Koizumi K, Kitagawa Y, Kawakami T, Yamanaka S, Okumura M and Yamaguchi K 2006 A general algorithm for calculation of Heisenberg exchange integrals J in multispin systems *Chem. Phys. Lett.* **432** 343–7

[42] Neese F (ORCA) 2007 *An Ab Initio, Density Functional and Semiempirical Program Package (v. 2.6-35)* (Bonn: Universität Bonn)

[43] VandeVondele J, Krack M, Mohamed F, Parrinello M, Chassaing T and Hutter J 2005 QUICKSTEP: fast and accurate density functional calculations using a mixed Gaussian and plane waves approach *Comput. Phys. Commun.* **167** 103–28

[44] Schäfer A, Horn H and Ahlrichs R 1992 Fully optimized contracted Gaussian basis sets for atoms Li to Kr *J. Chem. Phys.* **97** 2571–7

[45] Weigend F 2006 Accurate Coulomb-fitting basis sets for H to Rn *Phys. Chem. Chem. Phys.* **8** 1057–65

[46] Becke A D 1988 Density-functional exchange-energy approximation with correct asymptotic behavior *Phys. Rev.* A **38** 3098–100

[47] Lee C, Yang W and Parr R G 1988 Development of the Colle–Salvetti correlation-energy formula into a functional of the electron density *Phys. Rev.* B **37** 785–9

[48] Becke A D 1993 Density-functional thermochemistry. III: the role of exact exchange *J. Chem. Phys.* **98** 5648–52

[49] Sinnecker S, Rajendran A, Klamt A, Diedenhofen M and Neese F 2006 Calculation of solvent shifts on electronic g-tensors with the conductor-like screening model (COSMO) and its self-consistent generalization to real solvents (Direct COSMO-RS) *J. Phys. Chem.* A **110** 2235–45

[50] Goedecker S, Teter M and Hutter J 1996 Separable dual-space Gaussian pseudopotentials *Phys. Rev.* B **54** 1703–10

[51] Hartwigsen C, Goedecker S and Hutter J 1998 Relativistic separable dual-space Gaussian pseudopotentials from H to Rn *Phys. Rev.* B **58** 3641–62

[52] Dudarev S L, Manh D N and Sutton A P 1997 Effect of Mott–Hubbard correlations on the electronic structure and structural stability of uranium dioxide *Phil. Mag.* B **75** 613–28

[53] Dudarev S L, Botton G A, Savrasov S Y, Humphreys C J and Sutton A P 1998 Electron-energy-loss spectra and the structural stability of nickel oxide: an LSDA + U study *Phys. Rev.* B **57** 1505–9

[54] Perdew J P, Burke K and Ernzerhof M 1996 Generalized gradient approximation made simple *Phys. Rev. Lett.* **77** 3865–8

[55] Hornak V, Abel R, Okur A, Strockbine B, Roitberg A and Simmerling C 2006 Comparison of multiple amber force fields and development of improved protein backbone parameters *Proteins* **65** 712–25

[56] Wang J, Wolf R M, Caldwell J W, Kollman P A and Case D A 2004 Development and testing of a general amber force field *J. Comput. Chem.* **25** 1157–74

[57] Wang J, Wang W, Kollman P A and Case D A 2006 Automatic atom type and bond type perception in molecular mechanical calculations *J. Mol. Graph. Mod.* **25** 247–60

[58] Siu S W I, Vacha R, Jungwirth P and Böckmann R A 2008 Biomolecular simulations of membranes: physical properties from different force fields *J. Chem. Phys.* **128** 125103

[59] Jorgensen W L, Chandrasekhar J, Madura J D, Impey R W and Klein M L 1983 Comparison of simple potential functions for simulating liquid water *J. Chem. Phys.* **79** 926–35

[60] Lindahl E, Hess B and van der Spoel D 2001 GROMACS 3.0: a package for molecular simulation and trajectory analysis *J. Mol. Model.* **7** 306–17

[61] van der Spoel D, Lindahl E, Hess B, Groenhof G, Mark A and Berendsen H 2005 GROMACS: fast, flexible and free *J. Comput. Chem.* **26** 1701–18

[62] Laino T, Mohamed F, Laio A and Parrinello M 2005 An efficient real space multigrid QM/MM electrostatic coupling *J. Chem. Theory Comput.* **1** 1176–84

[63] Nosé S 1984 A unified formulation of the constant temperature molecular dynamics methods *J. Chem. Phys.* **81** 511–9

[64] Nosé S 1984 A molecular dynamics method for simulation in the canonical ensemble *Mol. Phys.* **52** 255–68

[65] Hoover W G 1985 Canonical dynamics: equilibrium phase-space distribution *Phys. Rev.* A **31** 1695–7

[66] Siegbahn P E M 2011 Recent theoretical studies of water oxidation in photosystem II *J. Photochem. Photobiol. B: Biol.* **104** 94–9

[67] Cox N and Messinger J 2013 Reflections on substrate water and dioxygen formation *BBA-Bioenergetics* **1827** 1020–30